Journal of Biomedical Optics 14(2), 024016 (March/April 2009)

Three-dimensional pointwise comparison of human retinal optical property at 845 and 1060 nm using optical frequency domain imaging

Yueli Chen[*]
Daina L. Burnes
Martijn de Bruin[†]
Mircea Mujat[‡]
Johannes F. de Boer[§]
Massachusetts General Hospital
Wellman Center for Photomedicine
40 Blossom Street
Boston, Massachusetts 02114

Abstract. To compare the optical properties of the human retina, 3-D volumetric images of the same eye are acquired with two nearly identical optical coherence tomography (OCT) systems at center wavelengths of 845 and 1060 nm using optical frequency domain imaging (OFDI). To characterize the contrast of individual tissue layers in the retina at these two wavelengths, the 3-D volumetric data sets are carefully spatially matched. The relative scattering intensities from different layers such as the nerve fiber, photoreceptor, pigment epithelium, and choroid are measured and a quantitative comparison is presented. OCT retinal imaging at 1060 nm is found to have a significantly better depth penetration but a reduced contrast between the retinal nerve fiber, the ganglion cell, and the inner plexiform layers compared to the OCT retinal imaging at 845 nm. [DOI: 10.1117/1.3119103]

Keywords: optical frequency domain imaging; optical coherence tomography; image segmentation and registration; optical scattering and absorption; retina.

Paper 08334R received Sep. 15, 2008; revised manuscript received Dec. 11, 2008; accepted for publication Jan. 15, 2009; published online Apr. 28, 2009.

1 Introduction

The human retina is composed of several tissue layers with varying optical properties, including scattering, absorption, and refractive index. While the retina primarily contains vertically aligned cells transparent to visible and near-IR light, the pigmented epithelial layer strongly scatters and absorbs light due to the presence of melanin. The posterior choroidal tissue, consisting primarily of vasculature, shows bloodlike wavelength-dependant absorption. The variation of the optical properties of the individual retinal layers produces the fundamental optical coherence tomography (OCT) image contrast. Recently, spectral or Fourier-domain optical coherence tomography (SD/FD-OCT) introduced a new principle with significantly improved sensitivity and scanning speed.[1–4] SD/FD-OCT can be realized either by a spectrometer-based[5–8] or a rapid tunable source[9–17] design. The later is known as optical frequency domain imaging (OFDI) or swept source OCT (SS-OCT). The capability of imaging retinal volumes at higher speeds enables for a reduction in measurement time and motion artifacts, making this second-generation OCT technology more appealing for retinal studies.

The majority of current OCT instruments for retinal imaging applications use wavelengths in the 845-nm region.[5,7,8,18–21] The advantages of imaging the posterior segment at 845 nm include minimal optical power loss from the double pass through the vitreous humor and the possibility for ultra-high-resolution imaging using available wideband optical sources.[22–25] More recently, an alternative wavelength centered at 1050 nm was investigated for retinal imaging.[26–34] The increasing interest in imaging at this wavelength is primarily due to the apparent improvement in depth penetration into the choroid compared to 845 nm. Other advantages include no visibility of the scanning beam to the subject and improved image quality in patients with cataracts.[29] Comparison studies of these two approaches were reported by Povožay et al.[26] and Unterhuber et al.[27] using time-domain systems and by Lee et al.[28] using SD-OCT at 845 nm and OFDI at 1060 nm. Clinical studies for these two wavelengths have also been reported.[33,34]

To increase our understanding of the optical properties and the OCT contrast mechanisms of retinal structures, it is important to quantitatively investigate the backscattered intensity distribution within the individual retinal segments. Hammer et al.[35] systematically studied the optical scattering of four posterior eye segments: the neural retina, the retinal pigment epithelium (RPE), the choroid, and the sclera. Scattering and absorption coefficients (μ_s, μ_a) were determined *in vitro* from bovine/porcine samples using a visible to 1064-nm spectral range. The study was also followed by an A-line analysis on OCT data.[36] In this paper, we directly compare the optical scattering properties from retinal layers scanned *in vivo* at the two wavelengths. Two equivalent OFDI systems at 1060 and 845 nm were used to image the same human subject, generating two sets of volumetric image data. A compre-

---

[*] Present address: Department of Electrical Engineering and Computer Science and Research Laboratory of Electronics, Massachusetts Institute of Technology, Cambridge, MA 02139 and New England Eye Center, Tufts Medical Center, Boston, MA 02116.

[†] Academic Medical Center, Meibergdreef 9, Amsterdam, The Netherlands.

[‡] Physical Sciences Inc., 20 New England Business Center, Andover, MA 01810.

[§] Department of Physics, Rm T0.67, VU University, De Boelelaan 1081, Amsterdam, The Netherlands, E-mail: jfdeboer@few.vu.nl.

1083-3668/2009/14(2)/024016/5/$25.00 © 2009 SPIE

hensive signal-processing algorithm was developed to facilitate a point-based quantitative comparison of the optical backscattered signal from the layered retinal structures.

2 Material and Methods

2.1 *Imaging Systems and Acquisition*

OFDI systems at 845 and 1060 nm were constructed for *in vivo* retinal imaging at a 30 kHz A-line rate. Both systems employed a linear cavity and a polygon-based wavelength-tuning filter. The 1060-nm system has a peak wavelength at 1060 nm and a −3-dB bandwidth of 60 nm. The 845-nm system has a peak wavelength at 845 nm and a bandwidth of 40 nm. The experimental axial resolutions in air were about 11 and 12.5 μm for the 845- and 1060-nm systems, respectively. The beam diameter on the pupil was 1.8 mm defined by $1/e^2$ beam width. The sample arm incident power was 1.7 mW and 460 μW for the 1060- and 845-nm systems, respectively. Using a partial reflector with known attenuation in the sample arm, we measured the sensitivity of the two systems. For the 845-nm system, the sensitivity was 93 dB. For the 1060-nm system, the sensitivity was 102 dB. A healthy male subject was imaged sequentially on the same day with the two systems, using the same optical human interface. A green light spot was presented as a fixation target. The pupil was monitored with an IR viewer to detect vignetting during the measurement. To estimate the beam size on the pupil, the focus size in the eye and the confocal parameter, the numerical aperture (NA) of the fiber encapsulating 86.5% of the beam energy was experimentally determined to be 0.088. Based on this fiber NA, the collimator focal length of 25 mm, the imaging lens focal length of 60 mm, and the Volk lens focal length of 25 mm, the beam radius on the eye was 0.9 mm. The focal radii were 5.0 and 6.2 μm assuming an eye length of 24 mm with $n=1.33$ for 845 and 1060 nm, respectively. The confocal parameters in the retina ($n=1.38$)) were 256 and 314 μm for 845 and 1060 nm, respectively. The fringe signal was digitized by an acquisition system with a sampling rate of 33 MHz and a 12-bit resolution. A previously described OFDI signal-processing algorithm for wavelength mapping and dispersion compensation was employed for both acquisitions.[12] The acquired images had a pixel volume of $512\times228\times512$ along the X (fast scanning axis), Y (slow scanning axis), and Z (depth axis) axes, respectively. The two systems also had a similar depth sensitivity decay due to the finite instantaneous laser line width of 6 dB over 2 mm in depth. The retinal images were acquired with the zero delay reference below the RPE to enhance the signal at large depths.

2.2 *Three-Dimensional Image Process*

2.2.1 *Coregistration of the two volumetric data sets*

To accurately compare two data sets, the image sets were spatially aligned. For this purpose, an en-face-based registration method was first employed. The en-face or XY 2-D plane was generated by integrating along the depth direction. Sixteen salient point pairs matching vascular branching features were manually selected on both en-face images. A local 2-D cross-correlation around each landmark region was calculated to refine the XY concurrent points. A second-order polynomial transformation was calculated to transform one set of points to its concurrent matched points, and this transformation was applied to the entire 3-D data set. A cubic interpolation was used to calculate the transformed pixel intensity for the registered image data set. Both image volumes were cropped to include only the maximum overlapping rectangular volume, resulting in a volume size of $397\times200\times225$ on the X, Y, and Z axes respectively.

For depth coregistration, segmentation of the retinal layers was employed to enable the alignment of A-line pairs at specific locations in depth. To match an A-line in one data set to its corresponding A-line in its spatially aligned data set, two point pairs are required. These point pairs were found by segmenting two prominent boundaries: the surface of the retinal nerve fiber layer (RNFL) and the junction between the photoreceptor inner and outer segment (IS/OS). A linear transformation based on these point pairs coregistered the volumes in depth.

2.2.2 *Quantitative comparison*

The incident power of the 1060-nm system was 5.7 dB more than that of the 845-nm system. The double-pass attenuation by the vitreous humor for the 1060-nm light was approximately 3 to 4 dB more than for the 845-nm light. Thus, the signal at 1060 nm is effectively larger by 1.7 to 2.7 dB. To ensure a proper comparison, the relative positions of the retinas at each imaging wavelength with respect to the zero delay reference was within 200 μm. The depth decay profiles of the two systems were similar. Within the imaging depth range of 100 to 700 μm where the intensity comparison was performed, the signal intensity decay was about 0.25 dB/100 μm. The effect of the sensitivity decay to the relative scattering comparison is small and normalization with regard to the sensitivity decay function was not performed. To compare the intensities reflected from the retinal layers at both wavelengths, the total power reflected from the retinal volume delineated by the RNFL and the OS layer was calculated. The 1060-nm power was 2 dB larger. To facilitate a relative quantitative comparison of the layers, the 1060-nm intensities were normalized to the 845-nm intensities by subtracting 2 dB.

A quantitative approach was taken to analyze the relative scattering properties of all the retinal layers. Three-dimensional segmented volumes of different retinal layers were created by manual selection and interpolation over five sequential OCT frames. The preceding approach was repeated three times at different locations, resulting in three separate five-frame layer segmentation volume clusters to estimate the standard deviation. Since both data sets were spatially aligned, the volumes can be directly overlaid on each data set without manipulation. Each volume consists of a variable number of pixels (200 to 750), representing the scattering intensity from that individual retinal layer. The average scattering intensities from each layer at both wavelengths were calculated, enabling a direct quantitative signal comparison. Mean and variance were calculated based on the mean of each cluster. The mean intensity was calculated from the linear intensity scale and then converted to decibels. The variance was estimated from the calculated mean intensity in decibel units.

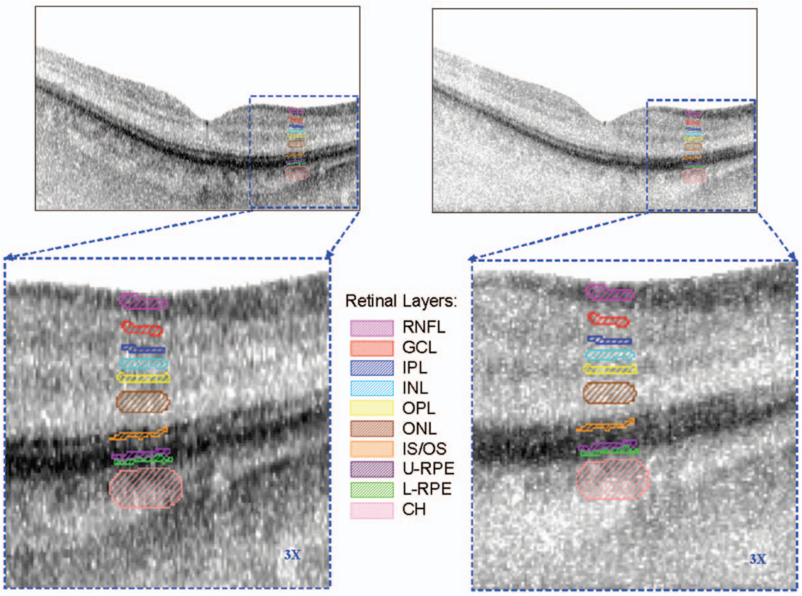

Fig. 1 Typical pointwise matched frame (left: 1060 nm, right: 845 nm). The cutout shows a 3× enlarged view of the retinal layers; color-coded overlays show the areas in which the backscattered intensity was calculated for each layer.

3 Results and Discussion

Figure 1 shows a single pointwise matched frame with the overlaid retinal layer segmentation volumes. The average intensity within each retinal layer volume is plotted in decibel units, as shown in Fig. 2, demonstrating the relative scattering intensities for the two wavelengths. The noise floor at both wavelengths was below 70 dB. The red horizontal line in Fig. 2 is the average intensity within the retinal volume delineated by the RNFL and the OS layer, providing relative contrast of the different retinal layers. The respective average scattering intensities and the standard deviations of each layer are listed in Table 1.

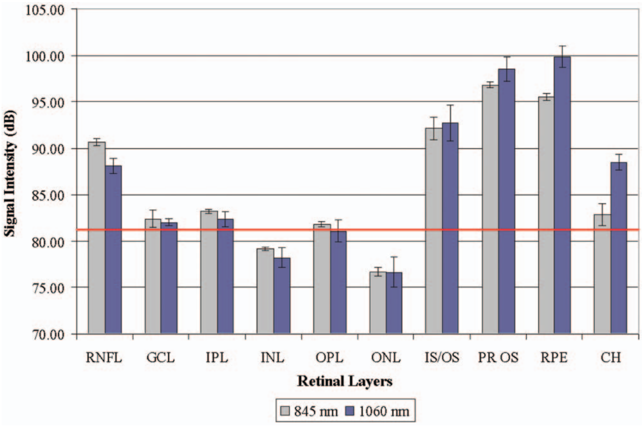

Fig. 2 Measured mean backscattered intensity from each retinal layer volume. The horizontal line at 81 dB is the mean intraretinal backscattered intensity. RNFL, retinal never fiber layer; GCL, ganglion cell layer; IPL, inner plexiform layer; INL, inner nuclear layer; OPL, outer plexiform layer; ONL, outer nuclear layer; IS/OS, photoreceptor inner segment/outer segment junction; U-RPE, upper retinal pigment epithelium; L-RPE, lower retinal pigment epithelium; CH, choroid.

The most striking differences between the contrast at 845 and 1060 nm are the 2.6-dB smaller reflected intensity in the RNFL and the 5.6-dB larger reflected intensity in the shallow choroidal tissue at 1060 nm as compared to 845 nm. Reflected intensities in the GCL, IPL, INL, OPL, ONL, and the boundary between the inner and outer segments of the photoreceptors are very similar. A major difference develops in the RPE. To obtain a more detailed attenuation profile in the RPE region, the layer corresponding to the tip of the RPE and the deeper portion was segmented in two, an upper RPE (U-RPE)

Table 1 Mean backscattered intensity and variance for each retinal layer at 845 and 1060 nm in decibel units. (dB).

	845 nm (dB)		1060 nm (dB)	
Layer	Mean	Std Dev	Mean	Std Dev
RNFL	90.66	0.37	88.09	0.78
GCL	82.42	0.96	82.04	0.40
IPL	83.22	0.26	82.37	0.78
INL	79.19	0.18	78.20	1.04
OPL	81.87	0.26	81.09	1.19
ONL	76.73	0.47	76.67	1.65
IS/OS	92.15	1.18	92.73	1.96
U-RPE	96.81	0.33	98.56	1.34
L-RPE	95.55	0.38	99.88	1.13
CH	82.87	1.23	88.51	0.84

Table 2 The relative contrast or backscattered intensity difference between adjacent retinal layers for 845 and 1060 nm in decibel.

λ	RNFL-GCL	GCL-IPL	IPL-INL	INL-OPL	OPL-ONL	ONL-ISOS	ISOS-U-RPE	L-RPE-Choroid
845 nm	8.24	−0.80	4.03	−2.68	5.14	−15.42	−4.66	12.68
1060 nm	6.05	−0.33	4.17	−2.89	4.42	−16.06	−5.83	11.37

and a lower RPE (L-RPE). At the L-RPE the reflected intensity at 1060 nm is 4.3 dB larger. This suggests that the thin melanin rich RPE tissue, with strong wavelength-dependent absorption, impacts the sensitivity enhancement observed in the choroidal tissue at 1060-nm light the most. As demonstrated from the scattering and absorption measurements by Hammer et al.,[35] the scattering coefficient μ_s is relatively constant for the RPE and only slightly decreases within the intraretinal layers from 780 to 1064 nm. Retinal tissue anisotropy further reduces the net contribution of μ_s to the total attenuation; however, the absorption of RPE is approximately four times greater at 780 than at 1064 nm. Based on the *in vitro* measurement by Hammer et al. and assuming a 10-μm RPE thickness, the calculated round-trip attenuation yields an intensity difference of 2.4 dB following the RPE attenuation. This calculation is less than our *in vivo* measurement finding of 4.3 dB. The backscattered intensity (Table 1 and Fig. 2) suggest that the increased attenuation of 845-nm light likely begins at a shallower depth (IS/OS junction) before the RPE. From Table 1 we conclude also that 4.3 dB of the 5.6-dB intensity difference for the two wavelengths at the shallow choroid can be attributed to the light path from the photoreceptor layer to and including the RPE.

An important aspect for 3-D volumetric image data of the human retina is segmentation of the different retinal layers for quantitative analysis, e.g., for the automated determination of RNFL thickness maps.[37,38] Better contrast between retinal layers improves the robustness of these segmentation algorithms. Table 2 shows the scattering intensity difference or relative contrast between individual retinal layers at 845 and 1060 nm. The 1060-nm acquisition wavelength has a significantly better sensitivity in deeper layers, but from Table 2 we can conclude that the 845-nm wavelength produces an overall better contrast at the inner-retinal layers, particularly between the RNFL and the GCL layers. At 845 nm, the relative contrast between RNFL and GCL is 8.24 dB, 2.2 dB more than for 1060 nm. Therefore segmentation algorithms for the RNFL and GCL might perform better for 845 nm wavelength data. The relative contrast between the GCL and IPL was only 0.33 dB, making the two layers difficult to discern in 1060-nm wavelength data.

4 Conclusions

Finely matching the reflectivity of retinal layers from equivalent OFDI systems at two separate acquisition wavelengths enables a quantitative comparison of optical properties such as scattering and attenuation. The relative reflectivity at 845 and 1060 nm of nine intraretinal layers and the choroid were measured and compared. The results indicate a relatively weaker signal intensity in the RNFL (−2.6 dB) for the 1060-nm images as compared to the 845-nm images, but a significantly stronger signal return from the RPE (+4.3 dB) and choroid (at least +5.6 dB). OFDI imaging at the alternative 1060-nm wavelength reduces the contrast between the RNFL and the GCL/IPL intraretinal layers, but significantly increases the signal at larger depths.

Better contrast between RNFL and GCL from 845-nm OFDI images might improve the robustness of segmentation algorithms to obtain RNFL layer thickness. It might be difficult to segment between GCL and IPL for 1060-nm OFDI retinal data. The quantitative reflected intensity comparison at the photoreceptor and RPE layers suggests the absorption from these tissue structures results in larger sensitivity degradation of 845-nm light at the choroid.

Acknowledgments

This research was supported in part by research grants from the National Institutes of Health (R01-RR019768 and R01-EY014975) and the Department of Defense (F4 9620-01-1-0014).

References

1. T. Mitsui, “Dynamic range of optical reflectometry with spectral interferometry,” *Jpn. J. Appl. Phys.* **38**(10), 6133–6137 (1999).
2. R. Leitgeb, C. K. Hitzenberger, and A. F. Fercher, “Performance of Fourier domain vs. time domain optical coherence tomography,” *Opt. Express* **11**(8), 889–894 (2003).
3. J. F. de Boer, B. Cense, B. H. Park, M. C. Pierce, G. J. Tearney, and B. E. Bouma, “Improved signal-to-noise ratio in spectral-domain compared with time-domain optical coherence tomography,” *Opt. Lett.* **28**(21), 2067–2069 (2003).
4. M. A. Choma, M. V. Sarunic, C. H. Yang, and J. A. Izatt, “Sensitivity advantage of swept source and Fourier domain optical coherence tomography,” *Opt. Express* **11**(18), 2183–2189 (2003).
5. A. F. Fercher, C. K. Hitzenberger, G. Kamp, and S. Y. El-Zaiat, “Measurements of intraocular distances by backscattering spectral interferometry,” *Opt. Commun.* **117** 43–48 (1995).
6. G. Hausler and M. W. Lindner, “Coherence radar and spectral radar—new tools for dermatological diagnosis,” *J. Biomed. Opt.* **3**(1), 21–31 (1998).
7. M. Wojtkowski, R. Leitgeb, A. Kowalczyk, T. Bajraszewski, and A. F. Fercher, “In vivo human retinal imaging by Fourier domain optical coherence tomography,” *J. Biomed. Opt.* **7**(3), 457–463 (2002).
8. N. Nassif, B. Cense, B. H. Park, M. C. Pierce, S. H. Yun, B. E. Bouma, G. J. Tearney, T. C. Chen, and J. F. de Boer, “In vivo high-resolution video-rate spectral-domain optical coherence tomography of the human retina and optic nerve,” *Opt. Express* **12**(3), 367–376 (2004).
9. F. Lexer, C. K. Hitzenberger, A. F. Fercher, and M. Kulhavy, “Wavelength-tuning interferometry of intraocular distances,” *Appl. Opt.* **36**(25), 6548–6553 (1997).
10. B. Golubovic, B. E. Bouma, G. J. Tearney, and J. G. Fujimoto, “Optical frequency-domain reflectometry using rapid wavelength tuning of a Cr/sup 4+/:forsterite laser,” *Opt. Lett.* **22**, 1704–1706 (1997).
11. S. R. Chinn, E. A. Swanson, and J. G. Fujimoto, “Optical coherence tomography using a frequency-tunable optical source,” *Opt. Lett.* **22**, 340–342 (1997).

12. S. H. Yun, G. J. Tearney, J. F. de Boer, N. Iftimia, and B. E. Bouma, "High-speed optical frequency-domain imaging," *Opt. Express* **11**(22), 2953–2963 (2003).
13. M. A. Choma, K. Hsu, and J. A. Izatt, "Swept source optical coherence tomography using an all-fiber 1300-nm ring laser source," *J. Biomed. Opt.* **10**(4), 044009 (2005).
14. R. Huber, M. Wojtkowski, K. Taira, J. G. Fujimoto, and K. Hsu, "Amplified, frequency swept lasers for frequency domain reflectometry and OCT imaging: design and scaling principles," *Opt. Express* **13**(9), 3513–3528 (2005).
15. R. Huber, M. Wojtkowski, and J. G. Fujimoto, "Fourier domain mode locking (FDML): a new laser operaing regime and applications for optical coherence tomography," *Opt. Express* **14**(8), 3225–3237 (2006).
16. W. Y. Oh, S. H. Yun, B. J. Vakoc, G. J. Tearney, and B. E. Bouma, "Ultrahigh-speed optical frequency domain imaging and application to laser ablation monitoring," *Appl. Phys. Lett.* **88**(10), 103902 (2006).
17. H. Lim, J. F. de Boer, B. H. Park, E. C. W. Lee, R. Yelin, and S. H. Yun, "Optical frequency domain imaging with a rapidly swept laser in the 815–870 nm range," *Opt. Express* **14**(13), 5937–5944 (2006).
18. S. Yazdanfar, A. M. Rollins, and J. A. Izatt, "Imaging and velocimetry of the human retinal circulation with color Doppler optical coherence tomography," *Opt. Lett.* **25**(19), 1448–1450 (2000).
19. S. Yazdanfar, A. M. Rollins, and J. A. Izatt, "In vivo imaging of human retinal flow dynamics by color Doppler optical coherence tomography," *Arch. Ophthalmol. (Chicago)* **121**(2), 235–239 (2003).
20. H. Lim, M. Mujat, C. Kerbage, E. C. Lee, Y. Chen, T. C. Chen, and J. F. de Boer, "High-speed imaging of human retina in vivo with swept-source optical coherence tomography," *Opt. Express* **14**(26), 12902–12908 (2006).
21. V. J. Srinivasan, R. Huber, I. Gorczynska, J. G. Fujimoto, J. Y. Jiang, P. Reisen, and A. E. Cable, "High-speed, high-resolution optical coherence tomography retinal imaging with a frequency-swept laser at 850 nm," *Opt. Lett.* **32**(4), 361–363 (2007).
22. W. Drexler, U. Morgner, F. X. Kartner, C. Pitris, S. A. Boppart, X. D. Li, E. P. Ippen, and J. G. Fujimoto, "In vivo ultrahigh-resolution optical coherence tomography," *Opt. Lett.* **24**(17), 1221–1223 (1999).
23. W. Drexler, U. Morgner, R. K. Ghanta, F. X. Kartner, J. S. Schuman, and J. G. Fujimoto, "Ultrahigh-resolution ophthalmic optical coherence tomography," *Nat. Med.* **7**(4), 502–507 (2001).
24. B. Cense, N. Nassif, T. C. Chen, M. C. Pierce, S. H. Yun, B. H. Park, B. E. Bouma, G. J. Tearney, and J. F. de Boer, "Ultrahigh-resolution high-speed retinal imaging using spectral-domain optical coherence tomography," *Opt. Express* **12**(11), 2435–2447 (2004).
25. M. Wojtkowski, V. J. Srinivasan, T. H. Ko, J. G. Fujimoto, A. Kowalczyk, and J. S. Duker, "Ultrahigh-resolution, high-speed, Fourier domain optical coherence tomography and methods for dispersion compensation," *Opt. Express* **12**(11), 2404–2422 (2004).
26. B. Povazay, K. Bizheva, B. Hermann, A. Unterhuber, H. Sattmann, A. F. Fercher, W. Drexler, C. Schubert, P. K. Ahnelt, M. Mei, R. Holzwarth, W. J. Wadsworth, J. C. Knight, and P. S. Russel, "Enhanced visualization of choroidal vessels using ultrahigh resolution ophthalmic OCT at 1050 nm," *Opt. Express* **11**(17), 1980–1986 (2003).
27. A. Unterhuber, B. Povazay, B. Hermann, H. Sattmann, A. Chavez-Pirson, and W. Drexler, "In vivo retinal optical coherence tomography at 1040 nm-enhanced penetration into the choroid," *Opt. Express* **13**(9), 3252–3258 (2005).
28. E. C. W. Lee, J. F. de Boer, M. Mujat, H. Lim, and S. H. Yun, "In vivo optical frequency domain imaging of human retina and choroid," *Opt. Express* **14**(10), 4403–4411 (2006).
29. B. Považay, B. Hermann, A. Unterhuber, B. Hofer, H. Sattmann, F. Zeiler, J. E. Morgan, C. Falkner-Radler, C. Glittenberg, S. Blinder, and W. Drexler, "Three-dimensional optical coherence tomography at 1050 nm versus 800 nm in retinal pathologies: enhanced performance and choroidal penetration in cataract patients," *J. Biomed. Opt.* **12**(4), 041211 (2007).
30. Y. Yasuno, Y. Hong, S. Makita, M. Yamanari, M. Akiba, M. Miura, and T. Yatagai, "In vivo high-contrast imaging of deep posterior eye by 1-μm swept source optical coherence tomography and scattering optical coherence angiography," *Opt. Express* **15**(10), 6121–6139 (2007).
31. R. Huber, D. C. Adler, V. J. Srinivasan, and J. G. Fujimoto, "Fourier domain mode locking at 1050 nm for ultra-high-speed optical coherence tomography of the human retina at 236,000 axial scans per second," *Opt. Lett.* **32**(14), 2049–2051 (2007).
32. Y. Chen, D. M. de Bruin, C. Kerbage, and J. F. de Boer, "Spectrally balanced detection for optical frequency domain imaging," *Opt. Express* **15**(25), 16390–16399 (2007).
33. D. M. de Bruin, D. L. Burnes, J. Loewenstein, Y. Chen, S. Chang, T. C. Chen, D. D. Esmaili, and J. F. de Boer, "In vivo three-dimensional imaging of neovascular age-related macular degeneration using optical frequency domain imaging at 1050 nm," *Invest. Ophthalmol. Visual Sci.* **49**(10), 4545–4552 (2008).
34. Y. Yasuno, M. Miura, K. Kawana, S. Makita, M. Sato, F. Okamoto, M. Yamanari, T. Iwasaki, T. Yatagai, and T. Oshika, "Visualization of sub-retinal pigment epithelium and sub-choroidal neovascularization morphologies of exudative macular diseases by optical coherence tomography with long wavelength probe," *Invest. Ophthalmol. Visual Sci.* **49**(50), 405–413 (2009).
35. M. Hammer, A. Roggan, D. Schweitzer, and G. Muller, "Optical-properties of ocular fundus tissues—an *in vitro* study using the double-integrating-sphere technique and inverse Monte-Carlo simulation," *Phys. Med. Biol.* **40**(6), 963–978 (1995).
36. M. Hammer, D. Schweitzer, E. Thamm, and A. Kolb, "Optical properties of ocular fundus tissues determined by optical coherence tomography," *Opt. Commun.* **186**(1–3), 149–153 (2000).
37. R. R. Bourne, F. A. Medeiros, C. Bowd, K. Jahanbakhsh, L. M. Zangwill, and R. N. Weinreb, "Comparability of retinal nerve fiber layer thickness measurements of optical coherence tomography instruments," *Invest. Ophthalmol. Visual Sci.* **46**(4), 1280–1285 (2005).
38. M. Mujat, R. C. Chan, B. Cense, B. H. Park, C. Joo, T. Akkin, T. C. Chen, and J. F. de Boer, "Retinal nerve fiber layer thickness map determined from optical coherence tomography images," *Opt. Express* **13**(23), 9480–9491 (2005).